

## Oxygen Ion Conductivity in Ceria-Based Electrolytes Co-doped with Samarium and Gadolinium

Alice V. Coles-Aldridge,<sup>a</sup> Richard T. Baker \*<sup>a</sup>

In a systematic study, two compositional series of ceria-based oxides, both co-doped with Sm and Gd, were synthesised using a low temperature method and evaluated as oxygen ion-conducting electrolytes for Intermediate Temperature Solid Oxide Fuel Cells (IT-SOFCs). Series one,  $\text{Ce}_{1-2x}\text{Sm}_x\text{Gd}_x\text{O}_{2-x}$ , had equal concentrations of Sm and Gd but varying total dopant concentration. Series two,  $\text{Ce}_{0.825}\text{Sm}_x\text{Gd}_{0.175-x}\text{O}_{1.9125}$ , had a fixed total dopant concentration but the Sm:Gd concentration ratio was varied. The materials were characterised using scanning and transmission electron microscopy, inductively coupled plasma mass spectrometry and X-ray diffraction. Impedance spectra were recorded on dense pellets of these materials. From these, total, bulk and grain boundary conductivities and capacitances along with activation energies, pre-exponential constants and enthalpies of ion migration and defect association were obtained. These gave a detailed insight into the fundamental conduction processes in the materials.  $\text{Ce}_{0.825}\text{Sm}_{0.0875}\text{Gd}_{0.0875}\text{O}_{1.9125}$  had the highest total ionic conductivity at temperatures of 550 °C and above and also demonstrated an enhanced conductivity with respect to its singly-doped parent compounds,  $\text{Ce}_{0.825}\text{Sm}_{0.175}\text{O}_{1.9125}$  and  $\text{Ce}_{0.825}\text{Gd}_{0.175}\text{O}_{1.9125}$ , at 400 °C and above. This compares favourably with previously-reported values and has promising implications for the development of IT-SOFCs.

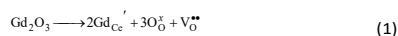
**Keywords:** Solid Oxide Fuel Cell; electrolyte; ceria; doping; ionic conductivity; activation energy

**Declarations of interest:** none

## Introduction

A promising technology to help address our global energy and environmental challenges are fuel cells, which convert chemical potential energy from a fuel and oxidant directly into electrical energy. Solid oxide fuel cells (SOFCs) in particular have high efficiencies, low emissions and fuel flexibility.<sup>1</sup> SOFCs are likely to have a large impact on energy conversion in the future, over a range of commercial applications from small domestic power units to large industrial facilities.<sup>2,3,4</sup> Currently, SOFCs typically operate at temperatures of 800 to 1000 °C.<sup>5</sup> By reducing this to intermediate temperatures (ITs) of between 500 and 750 °C, the auxiliary plant could be manufactured from low cost materials such as standard steels rather than expensive technical ceramics (e.g. precision-made alumina parts, lanthanum chromite-based interconnects). As well as allowing wider material choices, IT-SOFCs would reduce loss of performance and component degradation caused by electrode sintering, interfacial diffusion between electrolyte and electrodes and thermal stress.<sup>6,7</sup>

For successful implementation of IT-SOFCs, electrolytes with higher ionic conductivity are necessary. A partially-occupied oxygen ion sub-lattice containing a large number of interconnected and equivalent sites is required for high conductivity. This is obtained by doping the material with acceptor cations and so creating oxygen vacancies through which oxide ions are transferred by a hopping mechanism.<sup>8</sup> Yttria stabilised zirconia (YSZ) is the electrolyte material used in first generation SOFCs, but at intermediate temperatures, ceria-based electrolytes demonstrate higher oxide ion conductivity.<sup>9</sup> Reports have shown that ceria doped with trivalent rare earth ions – such as Gd as in Eqn. 1 - gives higher ionic conductivity than those doped with other elements, and in certain cases using multiple rare earth dopants gives rise to higher conductivity than the use of a single dopant.<sup>4,10</sup>



One interesting recent approach for optimising ionic conductivity is to search for an average dopant ionic radius which causes least distortion to the host lattice. This is reported to minimise both strain and activation energy for oxygen vacancy diffusion,  $E_\text{a}$ , and occurs when the repulsive elastic (related to dopant radius) and attractive electronic parts of the interactions between vacancies and dopant ions balance.<sup>11,12,13,14</sup> According to research by Andersson and co-workers using *ab initio* methods, this is the case for a hypothetical atomic number between 61 (Pm) and 62 (Sm).<sup>15</sup> Following this computational work, Omar et al. experimentally studied the energies of interaction between the oxygen vacancy and the dopant cations as a function of dopant ionic size. They concluded that the ionic conductivity was not a function solely of elastic strain, and therefore, a structure-ionic conductivity relationship based on critical radius was not sufficient to explain ionic conductivity behaviour in doped ceria.<sup>16</sup> Indeed, the local structure around dopants in CeO<sub>2</sub>, such as the formation by electrostatic attraction of clusters of vacancies and dopant ions, has

been reported to influence ionic mobility.<sup>17</sup> Connecting these concepts with experimental observations is valuable for electrolyte design.

Previous work by the authors on co-doped ceria electrolytes found that of the  $\text{Ce}_{0.8}\text{Sm}_x\text{Gd}_y\text{Nd}_z\text{O}_{1.9}$  materials studied (where  $x$ ,  $y$  and  $z = 0.2, 0.1, 0.0667$  or  $0$  and  $x + y + z = 0.2$ ),  $\text{Ce}_{0.8}\text{Sm}_{0.1}\text{Gd}_{0.1}\text{O}_{1.9}$  exhibited the highest conductivity between  $300\text{ }^\circ\text{C}$  and  $700\text{ }^\circ\text{C}$ .

<sup>4</sup> Wang and co-workers observed a higher conductivity for  $\text{Ce}_{0.85}\text{Gd}_{0.15-y}\text{Sm}_y\text{O}_{1.925}$  ( $0.05 \leq y \leq 0.1$ ) than for  $\text{Ce}_{0.85}\text{Gd}_{0.15}\text{O}_{1.925}$  or  $\text{Ce}_{0.85}\text{Sm}_{0.15}\text{O}_{1.925}$  between  $500$  and  $700\text{ }^\circ\text{C}$ .<sup>18</sup> This was attributed to the suppression of the ordering of oxygen vacancies leading to a lower  $E_a$  for the co-doped than for singly doped ceria. Dikmen and co-workers also found a four-fold increase in conductivity for  $\text{Ce}_{0.8}\text{Gd}_{0.2-x}\text{Sm}_x\text{O}_{2.6}$  at  $700\text{ }^\circ\text{C}$  for  $x = 0.1$  over  $x = 0$ . Greater increases were observed at the lower temperatures of  $500$  and  $600\text{ }^\circ\text{C}$ .<sup>19</sup> However, using La or Nd as co-dopants with Gd failed to surpass the conductivity of the material co-doped with Sm and Gd, at  $700\text{ }^\circ\text{C}$ . Zając and Molenda demonstrated that  $\text{Ce}_{0.85}\text{Sm}_{0.075}\text{Gd}_{0.075}\text{O}_{2-x/2}$  had a higher bulk conductivity at  $700\text{ }^\circ\text{C}$  than the singly-doped parent compounds or the co-doped sample,  $\text{Ce}_{0.85}\text{Nd}_{0.075}\text{Gd}_{0.075}\text{O}_{2-x/2}$ .<sup>20</sup>

It is apparent from the prior work of the authors and the relevant literature that Sm and Gd as either single or co-dopants in ceria electrolytes enhance conductivity to a greater extent than other rare earth dopants. Therefore, it is worth conducting a detailed study of how the total dopant concentration and the ratio of these individual co-dopants affect ionic conductivity in ceria co-doped with Sm and Gd. In this work, two compositional series,  $\text{Ce}_{1-2x}\text{Sm}_x\text{Gd}_x\text{O}_{2-x}$  where  $x = 0.125, 0.1, 0.0875, 0.075$  or  $0.05$  and  $\text{Ce}_{0.825}\text{Sm}_x\text{Gd}_{0.175-x}\text{O}_{1.9125}$ , where  $x = 0, 0.035, 0.070, 0.0875, 0.105, 0.140$  or  $0.175$ , were synthesised using a low temperature citrate method known to give high purity nanopowders.<sup>3,4</sup> The composition, powder nanostructure and crystal phase of these products were studied as were the microstructure and ionic conductivity of the dense electrolyte bodies prepared from them. The results gave insight into how subtle changes in composition affect the parameters determining favourable performance for IT-SOFC electrolytes. It is hoped that they will also aid future computational work on these materials.

## Experimental

Five compositions of  $\text{Ce}_{1-2x}\text{Sm}_x\text{Gd}_x\text{O}_{2-x}$  where  $x = 0.05, 0.075, 0.0875, 0.1$  or  $0.125$ , (series one), named SG050, SG075, SG0875, SG100 and SG125, respectively, and seven compositions of  $\text{Ce}_{0.825}\text{Sm}_x\text{Gd}_{0.175-x}\text{O}_{1.9125}$  where  $x = 0, 0.035, 0.070, 0.0875, 0.105, 0.140$  or  $0.175$  (series two), named G000, G035, G070, SG0875 (common to both series), G105, G140 and G175, respectively, giving eleven samples in total, were prepared (see Table S1 for compositions and naming conventions). Powder and dense pellet preparation followed procedures established in the group.<sup>3,4</sup>  $0.1\text{ mol dm}^{-3}$  solutions of appropriate amounts of metal nitrate hexahydrates -  $\text{Ce}(\text{NO}_3)_3 \cdot 6\text{H}_2\text{O}$  (Acros Organics, 99.5 %),  $\text{Sm}(\text{NO}_3)_3 \cdot 6\text{H}_2\text{O}$  and  $\text{Gd}(\text{NO}_3)_3 \cdot 6\text{H}_2\text{O}$  (both from Acros Organics, 99.9 %) were made separately in deionised water and were stirred for 3 h to homogenise before being combined and stirred further. A  $0.2\text{ mol dm}^{-3}$  citric acid solution was made by dissolving anhydrous citric acid (Alfa Aesar, 99.5 %) in deionised water and stirring for 3 h prior to addition to the metal cation solution in the ratio of one mole of total metal cations to two moles of citrate. The resulting solution

was stirred for 12 h, heated to 80 °C and maintained under stirring for 24 h. Evolution of steam and gas resulted in a gel and finally a solid yellow foam. Thermal decomposition of the foam was carried out in a muffle furnace at 250 °C for 2 h and the resulting powder was calcined in the muffle furnace at 500 °C for 2 h. Heating and cooling rates were 2.5 °C min<sup>-1</sup> and 5 °C min<sup>-1</sup>, respectively. The powders were dry ground for 1 h at 400 rpm in a planetary ball mill (Fritsch Pulverisette 7)<sup>21</sup> using Nylon jars and 10 mm diameter zirconia balls with a powder to ball mass ratio of 1:10. Ball milling was suspended every 15 min. to recover powder from the walls of the jar. The eleven resulting milled nanopowder compositions underwent detailed characterisation.

To make sintered electrolyte pellets, the powders were uniaxially pressed at 200 MPa in a 25 mm (for impedance spectroscopy) or 10 mm (for examination using SEM) diameter, cylindrical stainless steel die. The pellets were sintered at 1450 °C for 4 h with heating and cooling rates of 2 °C min<sup>-1</sup> and 4 °C min<sup>-1</sup>, respectively and polished to a mirror finish.

XRD analysis of the samples was carried out using a PANalytical Empyrean diffractometer with CuK $\alpha$ <sub>1</sub> monochromatic radiation. The external standard used was high-grade silicon powder which allowed correction for instrumental broadening. Data were acquired at room temperature by scanning 2 $\theta$  from 10° to 100° with a step size of 0.017 ° and a step time of 0.95 s. The XRD patterns were fitted using Rietveld operations in the High Score Plus programme.

The nanopowders were dissolved in conc. nitric acid in Teflon-lined autoclaves at 160 °C for 8 h for analysis by ICP-MS using an Agilent 7500ce with Ar gas flows of 0.82 L min<sup>-1</sup> (carrier) and 0.2 L min<sup>-1</sup> (makeup). Sample solutions were taken into the nebuliser at a rate of approximately 1.0 mL min<sup>-1</sup>. Three runs for each sample were carried out and each mass was analysed in fully quantitative mode (three points per unit mass). <sup>140</sup>Ce, <sup>157</sup>Gd and <sup>147</sup>Sm were analysed in no gas mode. Calibration standards were prepared using single element 1000 mg L<sup>-1</sup> stock solutions for Ce, Gd and Sm (Qmx), diluted with 2% HNO<sub>3</sub> v/v (Aristar grade, Merck).

SEM images of the pellets were obtained using a JEOL JSM-6700F instrument equipped with a field emission gun and were used to carry out statistical grain size analyses on each sample. For SEM, polished pellets were thermally etched at 1400 °C, employing a dwell time of 1 min and the same ramp rates as those used in the sintering process. Samples were gold-coated to reduce charging. The areas of many grains (> 400) were measured using ImageJ software for each sample. A JEOL JEM-2011 instrument was used to acquire TEM images for crystallite size analysis and to record electron diffraction patterns from selected sintered pellets. Powder samples were prepared by submerging 3 mm holey carbon Cu grids in an ultrasonicated dispersion of the powder in acetone. The Cu grids were dried overnight. Dense pellets of SG0875 as prepared and after reduction in 5%H<sub>2</sub>/Ar at 1000 °C for 4 h were dimple-ground (Gatan Model 656 Dimple Grinder) with 6  $\mu$ m then 1  $\mu$ m diamond paste and finally ion milled (Gatan Model 691 Precision Ion Polishing System) to obtain an area with the thickness of a single grain for examination in the TEM.

The dimensions and masses of the sintered pellets were used to calculate their densities. These values were divided by the corresponding theoretical density,  $\rho_{XRD}$ , calculated from the crystallographic information obtained by XRD, to obtain the relative densities.

The chemical compositions of a representative sub-group of the sintered pellets after fracturing and polishing to 1  $\mu\text{m}$  were obtained by Wavelength Dispersive Spectroscopy in an SEM-based microprobe instrument. The instrument used was a JEOL JXA 8600 Superprobe. WDS analysis with an electron microprobe detector was carried out on polished sintered pellets using a beam current of 20 nA, accelerating voltage of 15 kV, take-off angle of 40° and beam diameter of 1–2  $\mu\text{m}$ . Standards for the rare earths were phosphates of Ce, Sm, Nd and Gd. The rare earths were measured on a LiF analysing crystal using the  $\text{L}\alpha$  emission line for Ce and  $\text{L}\beta$  lines for Sm, Nd and Gd.

Two-electrode impedance spectroscopy was performed on the electrolyte pellets (of diameter  $\sim 20$  mm and thickness  $\sim 1.5$  mm) using a Solartron 1260 FRA instrument. Electrodes of 12 mm diameter were deposited by screen printing Pt ink (inorganic-free, Engelhardt) on each side of the pellets and firing at 1000 °C for 1 h with heating and cooling rates of 2 °C  $\text{min}^{-1}$ . The resulting cells were placed in a tube furnace and impedance measurements were carried out under flowing pre-dried, synthetic air (50  $\text{ml min}^{-1}$ ) at intervals of 50 °C between 150 – 900 °C, during both heating and cooling ramps. An A.C. voltage of amplitude 100 mV (250 °C – 900 °C) or 500 mV (150 °C – 200 °C) was applied and the frequency was swept from 10 MHz to 1 Hz (the latter, higher value was used to improve signal to noise at the lowest measurement temperatures). At each measurement temperature, multiple spectra were recorded until there were no variations between them. ZView software (Scribner Associates, Inc.) was used to analyse the impedance spectra.

## Results and discussion

### 3.1. Powder Characterisation

After calcination, the products consisted of voluminous fragile, papery structures which yielded pale yellow nanopowders after milling. XRD patterns of the eleven  $\text{Ce}_{1-2x}\text{Sm}_x\text{Gd}_x\text{O}_{2-x}$  and  $\text{Ce}_{0.825}\text{Sm}_x\text{Gd}_{0.175-x}\text{O}_{1.9125}$  nanopowders are given in Figure 1(a). All peaks were assigned to the cubic Fluorite crystal structure,  $Fm-3m$ . There is no evidence of any other phases, indicating that the dopants are fully soluble in the cerium oxide lattice. Figure 1(b)–(d) present lattice parameter, crystallite size and relative density data as a function of mole fraction of Sm. The lattice parameter ( $a$ , determined by Rietveld refinement of the XRD data) increased from 5.4237 Å ( $\text{Ce}_{0.9}\text{Sm}_{0.05}\text{Gd}_{0.05}\text{O}_{1.95}$ ) to 5.4339 Å ( $\text{Ce}_{0.75}\text{Sm}_{0.125}\text{Gd}_{0.125}\text{O}_{1.875}$ ) for series one (equal co-dopant concentrations) and from 5.4245 Å ( $\text{Ce}_{0.825}\text{Gd}_{0.175}\text{O}_{1.9125}$ ) to 5.4322 Å ( $\text{Ce}_{0.825}\text{Sm}_{0.175}\text{O}_{1.9125}$ ) for series two (constant total dopant concentration). The increase

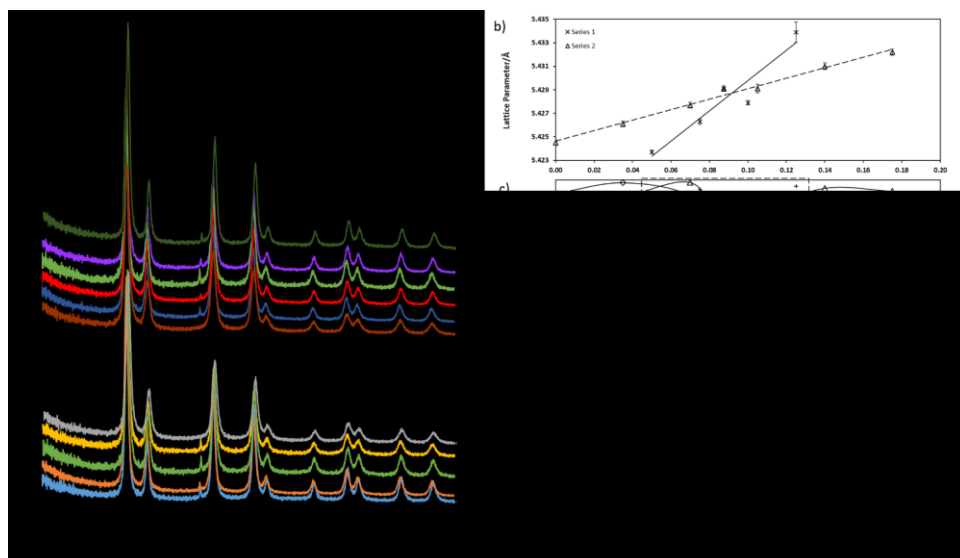


Figure 1. a) XRD patterns for powder samples of  $\text{Ce}_{1-2x}\text{Sm}_x\text{Gd}_x\text{O}_{2-x}$  (lower group) and  $\text{Ce}_{0.825}\text{Sm}_x\text{Gd}_{0.175-x}\text{O}_{1.9125}$  (upper group). \*Small peak at about  $45^\circ$  is due to the sample holder (main peak of Fe). Dependence on mole fraction of Sm in  $\text{Ce}_{1-2x}\text{Sm}_x\text{Gd}_x\text{O}_{2-x}$  (series one) and  $\text{Ce}_{0.825}\text{Sm}_x\text{Gd}_{0.175-x}\text{O}_{1.9125}$  (series two) of b) lattice parameter obtained from powder XRD; c) average crystallite size calculated from powder XRD data and TEM images in which series one data points are grouped for clarity and lines for series two are drawn as guides to the eye; d) relative density of pellets sintered at  $1450^\circ\text{C}$  for 4h.

in  $a$  for series one can be attributed to an increase in interatomic distances as the total dopant concentrations increase, leading to an expansion of the lattice. Both  $\text{Sm}^{3+}$  (1.079 Å) and  $\text{Gd}^{3+}$  (1.053 Å) are larger ions than  $\text{Ce}^{4+}$  (0.97 Å).<sup>22</sup> The increase in  $a$  for series two is due the progressive replacement of Gd by the larger Sm dopant ion. The lattice parameter shows a strong linear dependence when plotted against mole fraction of Sm for each composition (Figure 1(b)) indicating that Vegard's Law is obeyed in both series.<sup>22</sup> Table S1 summarises the lattice parameters and the average crystallite diameters ( $D_{\text{XRD}}$ ) of the eleven powders obtained from the XRD data.

Crystallite diameter was calculated from the extent of line broadening of the (111) diffraction peak using the Scherrer equation.<sup>23</sup> For both series it decreased as the Sm content - and hence average lanthanide ionic radius- increased, from 101 Å for  $\text{Ce}_{0.825}\text{Sm}_{0.035}\text{Gd}_{0.14}\text{O}_{1.9125}$  to 46 Å for  $\text{Ce}_{0.75}\text{Sm}_{0.125}\text{Gd}_{0.125}\text{O}_{1.875}$  (Figure 1(c)). It can be speculated that this might be caused by slower ionic diffusion during crystallite growth because of the slightly larger average cation radius caused by the increasing Sm content.

The  $D_{\text{XRD}}$  values are comparable to those reported in the previous work for similar samples made using the same synthesis method.<sup>24</sup> TEM images of each of the eleven samples were used to calculate the average diameter of the individual crystallites,  $D_{\text{TEM}}$ , (see Table S1 and Figure 1(c) and Figure 2(a-d)). In most cases,  $D_{\text{TEM}}$  was found to be slightly larger than  $D_{\text{XRD}}$ . This difference is normally attributed to the difficulty of reliably identifying very small nanocrystals in the TEM, especially since the crystallites are arranged in loosely agglomerated clusters – and therefore overlap in the images. This is generally the case for the series two samples, whose  $D_{\text{TEM}}$  and  $D_{\text{XRD}}$  values are, nevertheless quite similar. However, in series one, the trends in  $D_{\text{TEM}}$  and in  $D_{\text{XRD}}$  differed

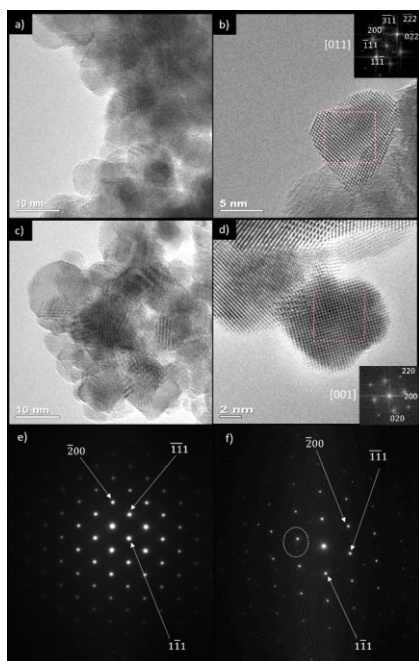


Figure 2: Medium and high magnification TEM images of SG075 (a, b) and G175 (c, d) nanopowders calcined at 500 °C for two hours. DDPs are inset in the high resolution images. Electron diffraction patterns for SG075 indexed to the fluorite structure viewed along the [011] zone axis for e) an oxidised and f) a reduced sample. The dashed ring in (f) encircles a main diffraction spot with two much fainter additional diffraction spots directly below.

from each other in that  $D_{TEM}$  increased and  $D_{XRD}$  decreased as Sm content increased. Importantly,  $D_{XRD}$  is a measure of crystallite size and  $D_{TEM}$  of particle size. The apparent discrepancy between them is likely to be due to the increasing misidentification of small clusters of multiple crystals as single particles in the intermediate-magnification TEM images as crystallite size decreased. Trends are highlighted with a dashed box and solid line for series one and two respectively in Figure 1(c).

Individual particles were seen by high resolution (HR)TEM (Figure 2(a-d)) to have excellent crystallinity with no evidence of crystallites containing multiple nanodomains. That is, the atomic arrangement appears to be uniform across each crystal and there are no regions within a crystal with different crystallographic structure or orientation. DDPs were obtained by performing a Fourier Transform on selected areas of the HRTEM images. Examples are inset in the corresponding images in Figure 2(b) and (d). These were indexed, respectively, to the ceria structure viewed in the [011] zone axis for  $Ce_{0.85}Sm_{0.075}Gd_{0.075}O_{1.925}$  and the [001] zone axis for  $Ce_{0.825}Gd_{0.175}O_{1.9125}$ .

Elemental analyses by ICP-MS are reported in Table S2. No major impurities were identified in any of the compositions, but there were discrepancies between the nominal stoichiometries and the ICP-MS results: the Ce concentration was consistently about 2 mol % lower than expected and the Sm and Gd concentrations were on average 0.6 and 1.4 mol % higher than expected,

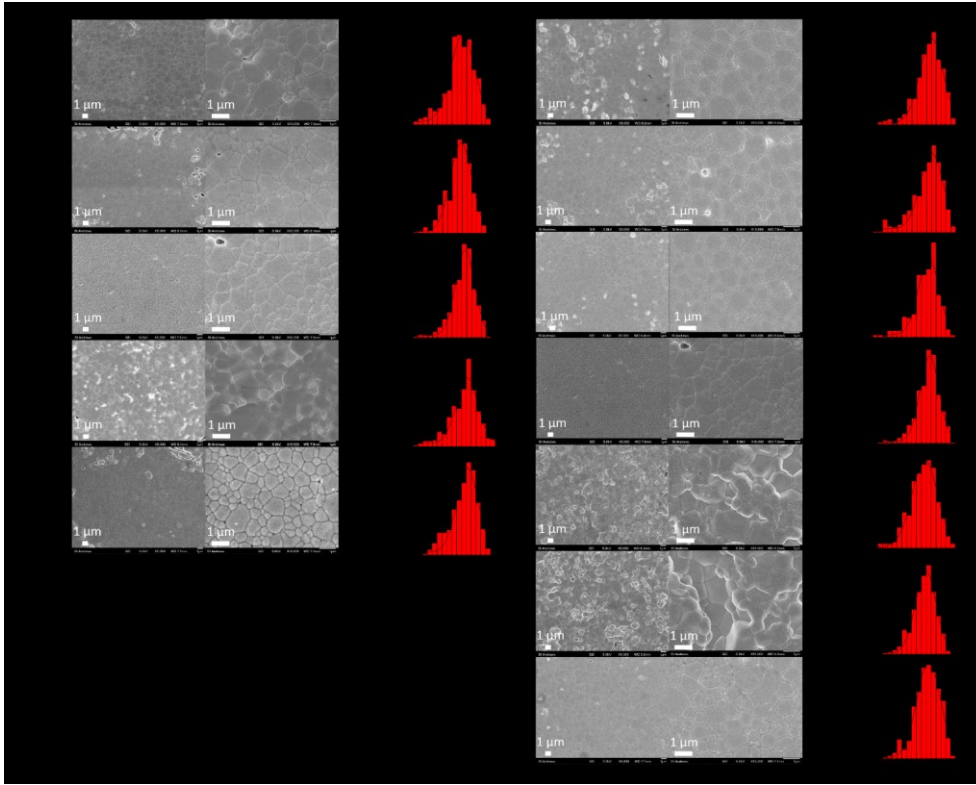


Figure 3. SEM images at intermediate and high magnifications alongside log histograms showing the grain area distributions for a) series one samples,  $Ce_{1-x}Sm_xGd_xO_{2-x}$ : i) SG050, ii) SG075, iii) SG0875, iv) SG100 and v) SG125 and b) for series two samples,  $Ce_{0.82}Sm_xGd_{0.175-x}O_{1.9125}$ : i) G000, ii) G035, iii) G070, iv) SG0875, v) G105, vi) S140 and vii) G175, sintered at 1450°C for 4h.

respectively. If we accept these results, because of their consistency, in series one, the expected increases in total dopant concentration would remain. In series two, the total dopant concentration is close to constant for each sample, meaning the oxygen vacancy concentration would be expected to be near-identical in each case. As a result, comparisons between samples could still be made based on the different individual dopant concentrations and identities. The slight excesses seen for Gd in particular have previously been attributed to the remaining 0.5 % in the 99.5 % pure cerium nitrate hexahydrate consisting primarily a gadolinium compound.<sup>25</sup> However, the microprobe analysis of the pellets in the next section challenges this explanation.

### 3.2 Pellet Characterisation

The relative densities of the sintered pellets ranged from 90.0 % for  $\text{Ce}_{0.9}\text{Sm}_{0.05}\text{Gd}_{0.05}\text{O}_{1.95}$  to 94.3 % for  $\text{Ce}_{0.825}\text{Sm}_{0.07}\text{Gd}_{0.105}\text{O}_{1.9125}$  (Figure 1(d)). There are no clear trends with mole fraction of Sm.

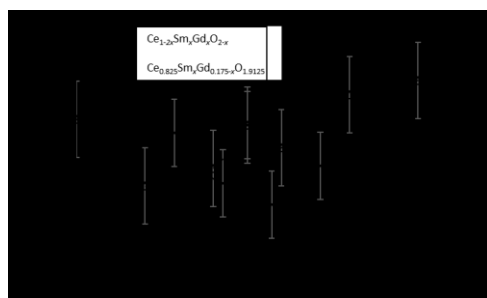


Figure 4. Average cross-sectional grain diameter as a function of mole fraction of Sm for  $\text{Ce}_{1-x}\text{Sm}_x\text{Gd}_{1-x}\text{O}_{2-x}$  and  $\text{Ce}_{0.825}\text{Sm}_x\text{Gd}_{0.175-x}\text{O}_{1.9125}$  sintered at 1450°C for 4 h. Lines are guides to the eye only. Errors bars are of +/- one standard deviation.

Formatted: Not Highlight

WDS was used for elemental analysis of a sub-set of the pellets and the values are reported in Table S2. No major impurities were identified in any of the compositions and the results are close to the nominal stoichiometries. The WDS results indicate that the discrepancies seen in ICP-MS are largely due to small software errors in calculating peak areas because of some overlap of the peaks of the analytically similar lanthanides, and not to the presence of significant impurities in the starting materials, as previously proposed.<sup>25</sup>

Figure 3 presents SEM images of the fired samples after polishing and thermal etching. Interlocking grains of typical, approximately hexagonal shape are observed. Normalised grain size distribution histograms are presented next to the corresponding images. These exhibit an approximately log-normal distribution of grain sizes with similar modal grain areas showing that grain growth was normal for all samples.<sup>24</sup> Average grain diameter against average ionic radius of the lanthanides is given in Figure 4. For series one there is no simple dependence of grain size on Sm content, as was also the case for relative density. For series two, grain diameter decreases on the first addition of Sm, and then increases monotonically with Sm content. This trend was not the same for relative density, however. Both  $\text{Sm}^{24}$  and  $\text{Gd}^{26}$  additions are reported to depress grain growth and grain size was high for G175 so it is not possible to give a simple interpretation of these data based on chemical composition.

In the SEM images all samples showed some porosity, accounting for their slightly lower than expected relative density. Grain growth could have been limited by these pores pinning the grain boundaries. This differs from the results of Kosinski and Baker where sintering conditions of 1450 °C for 4 h produced samples with lower porosity and larger grains but agrees with previous work on multiple doping using the same sintering conditions.<sup>24,25</sup> It is possible that the higher porosity than expected for these samples is due to oversintering. This phenomenon was reported by Liu et al<sup>27</sup> for  $\text{Ce}_{0.8}\text{Sm}_{0.1}\text{Nd}_{0.1}\text{O}_{1.9}$  sintered for 5 h at 1500°C and

(more markedly) 1600°C and proposed by Kosinski and Baker<sup>24</sup> for sintering conditions of 1450 °C for 6 h. Despite this, it should be noted that the grains were slightly larger in these studies than in the present work.

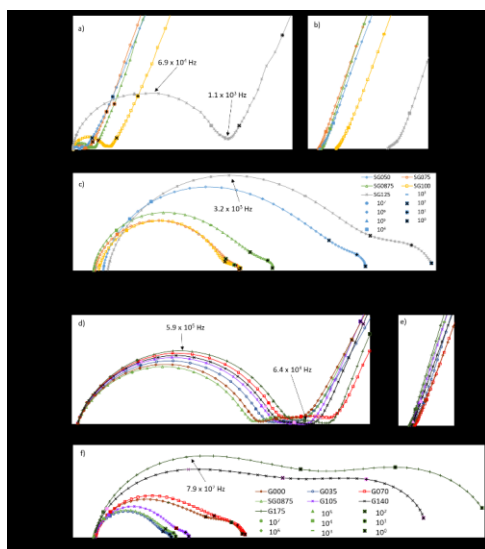


Figure 5. Nyquist plots for series one- SG050, SG075, SG0875, SG100 and SG125- at a) 250°C, b) 500°C and c) 750°C and for series two- G000, G035, G070, SG0875, G105, G140 and G175- at d) 250°C, e) 500°C and f) 750°C. Symbols represent the change in frequency decade, the keys for which are inset in (c) and (f). Lines joining datapoints are added as guides to the eye.

Formatted: Not Highlight

The electron diffraction patterns in Figure 2(e) and (f) are both consistent with the cubic fluorite crystal structure. There are no additional features in the diffraction pattern of the sample prepared in an oxidising environment (Figure 2(e)), indicating that there is no detectable defect ordering, nanodomain or superstructure formation. Since the sample should be close to fully oxidised, the  $Ce^{3+}$  concentration should be negligible. The oxygen vacancies present therefore would be due to the presence of the trivalent dopants, Sm and Gd, and, at room temperature, are likely to be mostly associated with them, in defect clusters. The fact that no spots were seen in this case suggests that the oxygen vacancies, and therefore the Sm and Gd dopants, are not ordered throughout the crystal lattice but randomly distributed. This and the absence of evidence of nanodomains of distinct crystal structure indicates that the material was of high phase purity and chemical homogeneity. When this sample is reduced, however, faint additional spots were observed (Figure 2(f)). In this sample,  $Ce^{3+}$  concentration would have been higher. The additional spots may be caused by additional oxygen vacancies which were able to order to some extent because the majority cation, Ce, is ubiquitous throughout the lattice and could have become reduced in any lattice position, giving rise to  $Ce^{3+}$  ions with which the oxygen ion vacancies could associate. Therefore, oxygen-deficient planes or nanodomains may have been formed which would give rise to the kind of additional spots seen in Figure 2(f). It appears then, that observable vacancy ordering only occurred when this doped ceria has been exposed to a reducing environment, which is not the case during the electrical measurements in this work.

XRD patterns of all of the  $\text{Ce}_{1-2x}\text{Sm}_x\text{Gd}_x\text{O}_{2-x}$  and  $\text{Ce}_{0.825}\text{Sm}_x\text{Gd}_{0.175-x}\text{O}_{1.9125}$  pellets are given in Figure S1. All peaks could be assigned to the cubic fluorite  $Fm-3m$  crystal structure. There was no evidence of any other phases indicating that, like the powders, the pellets were each single phase materials.

### 3.3. Electrical Properties

Impedance spectra are presented as Nyquist plots in Figure 5 for both series. Electronic conductivity can be considered to be negligible under the oxidising conditions used in this work. At low temperatures (150 – 400 °C) two arcs are visible in the spectra. The higher frequency arc is assigned to bulk (intra-granular) ionic conduction and the smaller arc at lower frequency to ionic conduction across the grain boundaries (inter-granular). These two arcs were each fitted using the ZView software to electronic subcircuit models consisting of a resistance in parallel with a Constant Phase Element (CPE). The equivalent circuit corresponding to the electrolyte response can be written  $(R_b\text{CPE}_b)(R_{gb}\text{CPE}_{gb})$ , where resistances,  $R$ , and CPEs, relate to electrolyte bulk,  $b$ , and electrolyte grain boundary,  $gb$ . Total, bulk and grain boundary conductivities were calculated from the resistances acquired from the impedance spectra, the area of the Pt electrodes and the thickness of the electrolyte pellets. At intermediate (450 – 550 °C) and high (600 – 900 °C) temperatures, the bulk arc was progressively obscured by the effect of the inductance of the apparatus and shifted above the operating frequency window of the spectrometer. Therefore, separate bulk and grain boundary conductivities were obtained from the spectra only for the lower temperatures, while total conductivities (bulk plus grain boundary) were obtained for all temperatures, since these can be obtained from the intercept with the  $Z'$  axis in the absence of the bulk arc. The smaller, low frequency arc at 750 °C can be assigned to electrode processes.

#### 3.3.1. Capacitances

Values of capacitance bulk ( $C_b$ ) and grain boundary ( $C_{gb}$ ) capacitances were extracted calculated from the characteristic frequency  $f_c$ , and resistance,  $R$ , of the corresponding arcs in the fits to the Nyquist plots, and these are presented in Figure 6. The absolute values and range of bulk capacitance,  $C_b$ , are similar for the two series and are of the same order as those previously reported for YSZ (0 - 10 mol %  $\text{Y}_2\text{O}_3$ ).<sup>28</sup> In series one,  $C_b$  showed a clear maximum at  $x = 0.0875$  for all temperatures at which it could be accurately measured (150 – 300 °C). At  $x = 0.0875$  (SG0875),  $C_b$  increased as temperature increased to a maximum of  $6.19 \times 10^{-11}$  F at 300 °C. However, for the other compositions, there is no such clear relationship with temperature. For series two, a similar peak in  $C_b$  was observed at the sample common to both series, SG0875, at most temperatures, where the Sm:Gd ratio was 50:50. The only exception to this was at 150 °C for which the maximum was shifted slightly to a neighbouring composition, G105. For series two, bulk capacitance generally increased with increasing temperature. The maxima at SG0875 in both series are interesting given that this composition also showed the highest conductivity at intermediate and high temperatures in series one and at all temperatures in series two (see below). The peaks in  $C_b$  for SG0875 coincide with peaks in bulk conductivity for the same material. However, the capacitances were measured at low temperatures ( $\leq 300$  °C) while peak conductivities were seen for SG0875 at both low and

Formatted: Highlight

Formatted: Highlight

Formatted: Highlight

Formatted: Subscript, Highlight

Formatted: Highlight

Formatted: Highlight

Formatted: Font: Italic

Formatted: Font: Italic, Subscript

Formatted: Font: Italic

Formatted: Highlight

Formatted: Highlight

Formatted: Highlight

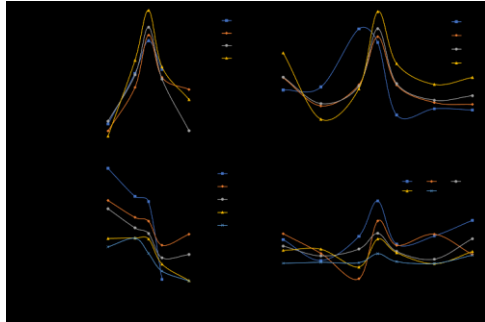


Figure 6. Bulk and grain boundary capacitances as a function of mole fraction of Sm,  $x$ , for a) and c) series one,  $Ce_{1-x}Sm_xGd_{0.2-x}O_{2-x}$ , and for b) and d) series two,  $Ce_{0.825}Sm_xGd_{0.175-x}O_{1.9125-x}$ .

higher temperatures (up to 900 °C). This is important because the majority of oxygen vacancies are expected to be trapped in defect clusters at the former, low temperatures, but to be free at temperatures above about 500 °C. This means that the peaks in bulk capacitance were measured in the presence of defect clusters while the peak in bulk conductivity persists even when these have been thermally dissociated. It is difficult, therefore, to relate the two, even though they coincide for the same sample composition. It may be possible, however, by considering the nature of capacitance in detail. The capacitance of a simple, ideal parallel plate capacitor is proportional to a geometric factor and to the permittivity of the material between the plates (Eqn. 2).

$$C = \epsilon_r \epsilon_0 \frac{A}{d} \quad (2)$$

where  $\epsilon_r$  is the relative permittivity between the plates,  $\epsilon_0$  is the dielectric constant (or permittivity of free space),  $A$  is area of overlap of the plates and  $d$  is the distance between the plates. The peaks seen in Figure 6 are not replicated in any of the physical properties of these series of materials which might be related to the geometric factor. Therefore, they appear to have been caused by variations in permittivity of the bulk material as sample composition was varied. Permittivity is itself linearly related to the susceptibility of a material to becoming electrically polarised by an applied electric field. Following this logic, sample SG0875 is the most easily bulk-polarised of these two series. Polarisation here involves reversible, short-range (approximately atomic or sub-atomic scale) displacement of charges; in this case, displacement of ionic nuclei and distortion of associated electron clouds in opposite directions. Importantly, this does not (necessarily) involve movement of ions between different lattice sites; the basic steps in both ionic conduction and defect dissociation. This would mean that SG0875 has a combination of ions arranged in such a way in its crystal lattice as to favour ease of polarisation, within these two compositional series. This polarisability might be described as the overall, or average, lability of the charges in the bulk of the material. It is speculative, but this might in turn be reasonably related to both ease and extent of migration of charge carriers and ease and extent of their dissociation from defect clusters. Therefore, a maximum in capacitance – and so in bulk polarisability – would indicate a favourable material composition

for bulk ionic conductivity, even if the capacitance had been measured at lower temperatures than those at which the material shows its favourable bulk conductivity.

Grain boundary capacitances,  $C_{gb}$ , for series one and two are also presented in Figure 6. These would normally be affected by the composition of the grain boundaries – which in high purity materials should be similar to that of the bulk – and the microstructure of the material. Usually, the largest effect on microstructure is that of grain size. The larger the grains, the fewer grain boundaries must be crossed by the ionic current and the higher the overall grain boundary capacitance. In series one and two, grain size did not vary much (Figure 4), but there is a loose correlation between grain size and the general trends in  $C_{gb}$ , with capacitance tending to decrease with increasing grain size (compare Figures 4 and 6). However, in addition to this, for series one, there was a general decrease in  $C_{gb}$  with increasing dopant mole fraction. On this trend, however, is superimposed a local maximum at SG0875. For series two, a peak in  $C_{gb}$  is also seen for SG0875 but otherwise the relative concentrations of Sm and Gd have no discernible correlation with  $C_{gb}$ . This suggests that the decreasing trend seen for series one is primarily due to the changes in total dopant concentration. This is an interesting result but further explanation is beyond the present study. In series one, then, the  $C_{gb}$  values appear to be the result of the combined effects of intrinsic (bulk) capacitance, giving rise to the peaks seen at  $x = 0.0875$ , microstructure and the effect of increasing total dopant concentration. The  $C_{gb}$  values for both series are towards the upper end of the range previously found for YSZ.<sup>28</sup> There are greater differences in  $C_{gb}$  than in  $C_b$  due to the influence of a combination of microstructural and compositional effects which are difficult to individually extract. For both series, the peak at SG0875 in both  $C_b$  and  $C_{gb}$  suggests a contribution of bulk properties to grain boundary capacitance.

### 3.3.2. Conductivities

Figure S2 displays Arrhenius-type plots of the total ( $\sigma_t$ ), bulk ( $\sigma_b$ ) and grain boundary ( $\sigma_{gb}$ ) conductivity for all of the samples in both series (SG0875 is common to both series so appears twice). Generally  $\sigma_{gb}$  was significantly higher than  $\sigma_b$ . Because of this,  $\sigma_t$  was determined essentially by  $\sigma_b$  for nearly all samples. The only exceptions to this were the samples of series one with low dopant concentrations, SG050 and SG075, at low measurement temperatures ( $\leq 300^\circ\text{C}$ ). This is because of the increase in bulk conductivity with decreasing total dopant concentration at low measurement temperatures (see below). The high  $\sigma_{gb}$  values indicate that the materials synthesised in this work had low levels of impurities since these tend to accumulate at grain boundaries and would have a particularly strong negative effect on  $\sigma_{gb}$ . Indeed, Si – the most problematic impurity in SOFC materials – is found to be below the ICP-MS detection limit (equivalent to 25 ppm in the solid samples) in the materials synthesised in this study and below 10 ppm in XPS for multiply-doped cerias prepared in the same way.<sup>29</sup>

In order to show clearly the differences between compositions,  $\sigma_b$ ,  $\sigma_{gb}$  and  $\sigma_t$  are plotted against temperature in Figure 7 in normalised form. The normalisations were carried out by dividing each conductivity value by the corresponding value for the relevant reference sample (SG075 for series one and G140 for series two) at the same temperature. The reference samples were chosen to maximise the clarity of the figures.

As can be seen in Figure 7(a), there is a clear decreasing trend in normalised  $\sigma_b$  as total dopant concentration increases, at all temperatures at which  $\sigma_b$  could be measured (150 – 400 °C). This is attributed to the decrease in the extent of defect association as dopant concentration decreases from SG125 to SG050.<sup>30</sup> Fewer defect complexes form when the dopants and oxygen vacancies are more dilute and this results in less trapping of these vacancies, so a greater number can participate in ionic conduction.<sup>8,24,26,30</sup> At 400 °C, thermal dissociation of these defects starts to become significant and the order of the samples in Figure 7(a) begins to change.

For series two (Figure 7(d)), in which total dopant concentration was kept constant at 0.175, the range of  $\sigma_b$  is much smaller than for series one, in which total dopant content was changed. Single doping with Sm (G000) and equal co-doping with Sm and Gd (SG0875) gave the highest  $\sigma_b$  at 150 and 200 °C, whilst between 250 and 400 °C, SG0875 clearly had the highest  $\sigma_b$ . Single doping with Gd (G175) gave the lowest  $\sigma_b$  between 150 and 400 °C. The four doubly-doped samples lie in between with their relative order varying as the temperature increased. The high values for SG0875 may be due to the equal concentration of Sm and Gd co-dopants giving a more favourable average ionic radius for oxygen ion mobility.<sup>31</sup> Overall, the differences in normalised  $\sigma_b$  in both series decreased as temperature increased.

For series one,  $\sigma_{gb}$  (Figure 7(b)) shows a broadly similar dependence on dopant concentration as did  $\sigma_b$ , suggesting that intrinsic (bulk) conductivity is an important factor in  $\sigma_{gb}$  for these samples. The main exception to this is that SG050 had only the third highest  $\sigma_{gb}$  between 150 and 350 °C and SG075 had the highest over this temperature range. As temperature increased, the normalised  $\sigma_{gb}$  values for series one converged and at 400 °C the order of the samples changed, probably because of the start of thermal dissociation of the defect clusters (see above). Also, since material at the grain boundaries is more disordered than in the bulk this “switchover” might be expected to happen at slightly lower temperatures than for  $\sigma_b$ , as does appear to be the case for series one.

In series two, the normalised  $\sigma_{gb}$  data (Figure 7(e)) showed a greater variation in sample order compared to the corresponding normalised  $\sigma_b$  values. G105 had the highest  $\sigma_{gb}$  between 150 and 300 °C and G035 and G105 had similar  $\sigma_{gb}$  values at 350 and 400 °C. SG0875 had the lowest  $\sigma_{gb}$  at all measurable temperatures (150 – 400 °C) despite having the highest bulk conductivity over this temperature range. Unlike for series one, no convergence in  $\sigma_{gb}$  was observed in series two as temperature increases.

These variations in grain boundary conductivity with composition cannot be simply accounted for by considering the grain size and density of the samples. The small relative size of the grain boundary arcs (hence the larger errors in Figure 7 (b) and (e)) and the small variations seen in relative density and in grain area across both sample series makes it difficult to interpret the differences in  $\sigma_{gb}$  values in terms of microstructural parameters. Also, the different chemical compositions are likely to have some effect on the properties of the grain boundaries.

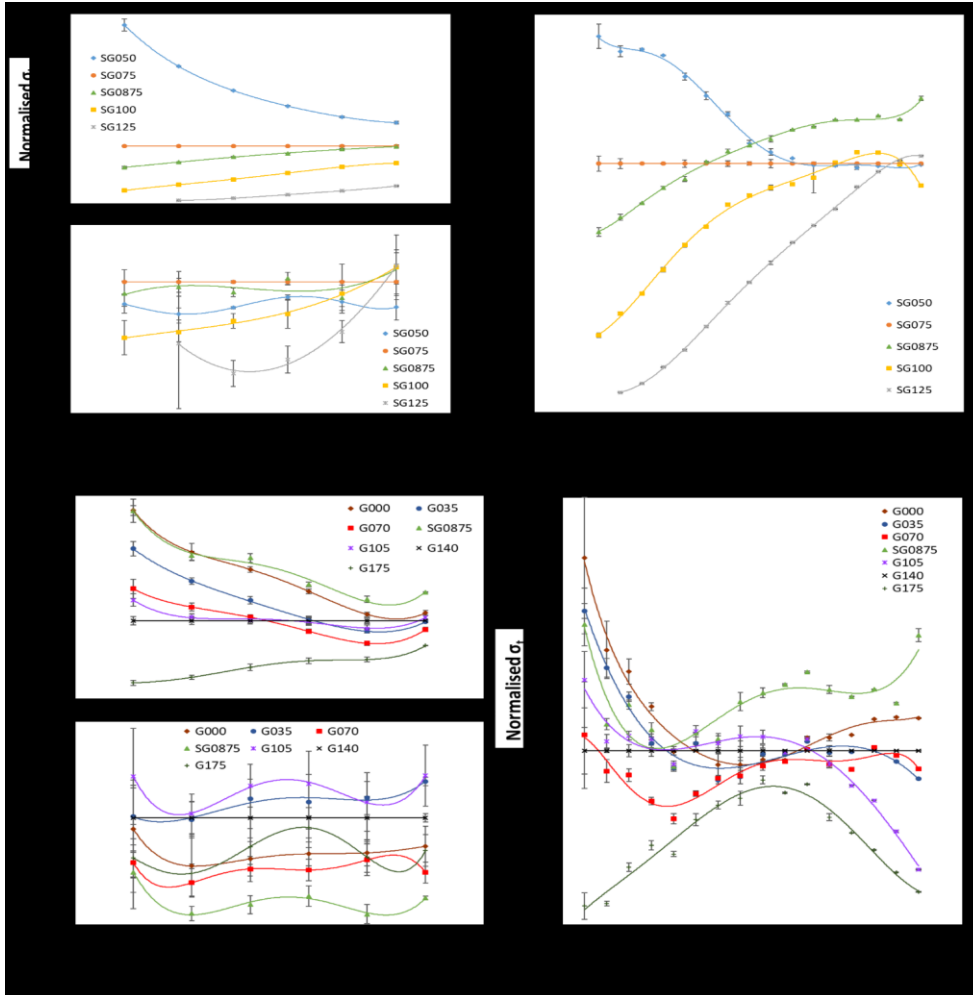


Figure 7. Plots of normalised (with respect to SG075) a) bulk conductivity, b) grain boundary conductivity and c) total conductivity vs. measurement temperature for series one,  $\text{Ce}_{1-x}\text{Sm}_x\text{Gd}_y\text{O}_{2-x-y}$ , and (normalised with respect to G140) d) bulk conductivity, e) grain boundary conductivity and f) total conductivity vs. measurement temperature for series two,  $\text{Ce}_{0.925}\text{Sm}_x\text{Gd}_{0.175-x}\text{O}_{1.9125-x}$ .

In Figure 7(c) and (f), normalised  $\sigma_t$  is plotted over the whole range of measurement temperatures, from 150 to 900 °C. For series one, between 150 and 350 °C the samples are arranged in the same order of increasing normalised  $\sigma_t$  as they are for  $\sigma_b$  in Figure 7(a). At 400 °C the order of SG075 and SG0875 is reversed but the values are very close and the remaining samples have the same order. This again indicates the relatively small effect of  $\sigma_{gb}$  on  $\sigma_t$  and therefore that  $\sigma_t$  is determined essentially by  $\sigma_b$ . The  $\sigma_t$  is lowest for SG125 up to 800 °C, for SG050 at 850 °C and for SG100 at 900 °C. The convergence in normalised  $\sigma_t$  as temperature increased is likely to be caused by the dissociation of defect complexes at high temperatures and means that the different defect

concentrations and overall oxygen ion mobilities resulting from the different total dopant concentrations of the series one samples had less impact on conductivity at the highest temperatures. This indicates that the spread in concentration of free oxygen vacancies at low temperature is greater than it is at high temperature, despite the expectation that all defect clusters should be dissociated at 900 °C. The highest  $\sigma_i$  values in series one were for SG050 between 150 and 500 °C and for SG0875 between 550 and 900 °C. The low temperature normalised  $\sigma_i$  values can be explained in the same way as the  $\sigma_b$  values. The fact that SG0875 had the highest  $\sigma_i$  at high temperatures is likely due to an optimal compromise between oxygen vacancy concentration and mobility. The important result that SG0875 had a higher conductivity than that previously reported for SG100 at all temperatures is technologically important given the drive to reduce SOFC operating temperatures and to develop IT-SOFCs for use between 500 and 750 °C.<sup>25</sup> Furthermore, in extended tests on the SG0875 sample,  $\sigma_i$  decreased by less than 0.6 % over 100 h.

The trends in  $\sigma_i$  observed for series two are less clear than for series one as the dopant concentration is now constant and the subtler variation in dopant ratio is the focus. As a result, normalised  $\sigma_i$  values covered a much smaller range in series two than in series one. In Figure 7(f), G175 had the lowest normalised  $\sigma_i$  at all temperatures which shows the detrimental effect of doping with Gd without Sm. This may be due to the smaller ionic radius of Gd<sup>3+</sup> and hence its preference for oxygen vacancies in the NN position as opposed to Sm<sup>3+</sup> which is larger and is reported to have no NN/NNN preference.<sup>15</sup> This may also be the reason for the general trend of increasing conductivity with increasing Sm content at low temperatures, where, at 200 and 250 °C, G070 is the only sample not in this order. As temperature increased, the NN preference of Gd would become less significant due to the higher thermal energy of the lattice. SG0875 had the highest total conductivity between 450 and 900 °C but the remaining five samples do not show clear trends and the order fluctuates as temperature changes. However, G000 had the highest normalised  $\sigma_i$  values between 150 and 300 °C and the second highest values between 650 and 900 °C. This reflects the high  $\sigma_i$  previously observed for single doping with Sm over a similar high temperature range.<sup>25</sup> Figure 7(f) shows a convergence in total conductivity values at intermediate temperatures which spread out at the temperature extremes, but not to the extent seen in series one at low temperatures, because of the effects of defect dilution. The  $\sigma_i$  values for series two do not mirror  $\sigma_b$  as closely as for series one. This may be due to the less significant changes in composition in series two meaning that microstructure has a greater relative influence.

The fact that SG0875 had the highest  $\sigma_i$  at intermediate temperatures is interesting given that there were maxima in bulk and grain boundary capacitances for this composition. As discussed in Section 3.3.1, this may imply that the capacitance values relate to a process fundamental to conductivity which becomes more apparent in the conductivity data only as temperature increases. These conductivity results provide further evidence that Sm-Gd co-doping can give rise to an improvement in conductivity over the singly-doped parent materials and, therefore, that the conductivity of co-doped cerias cannot always be interpreted simply as an average of the conductivities of the singly-doped parent materials, as was concluded in the computational study of Burbano *et al.*<sup>17</sup> From Figure 7, SG0875 had the highest total conductivity (higher than both parents, G000 and G175) at IT-SOFC working

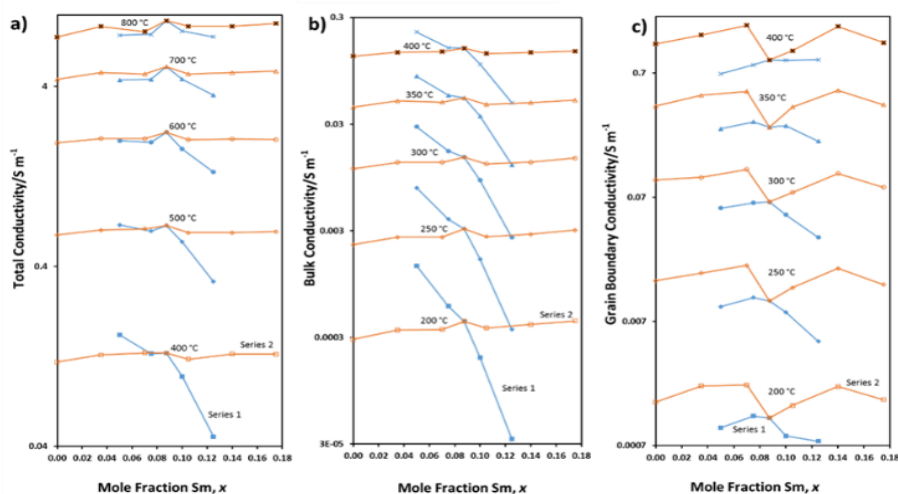


Figure 8. a) Total, b) bulk and c) grain boundary conductivity on a log scale as a function of mole fraction of Sm,  $x$ , for series one,  $Ce_{1-2x}Sm_xGd_{0.2-3x}O_{2-x}$  (blue) and series two,  $Ce_{0.825-0.175x}Sm_xGd_{0.175-x}O_{1.9125}$  (orange) at the temperatures indicated.

temperatures. A total dopant concentration for Sm-Gd co-doping of 17.5 mol % gave the best conductivity here and represented an increase in  $\sigma_t$  of 24 % at 600 °C (to  $2.23 \text{ S m}^{-1}$ ) compared to SG100, the previously reported most conducting composition at IT-SOFC working temperatures.<sup>25</sup> Using an equal concentration of Sm and Gd co-dopants gave a 9 % increase in  $\sigma_t$  at 600 °C compared to the next highest conducting sample (G105) in this series.

Figure 8 presents log plots of  $\sigma_b$ ,  $\sigma_{gb}$  and  $\sigma_t$  against sample composition for both series of compounds to show how the different combinations and concentrations of dopants affect conductivity at key SOFC temperatures. In both series, as temperature increases, a peak at  $x = 0.0875$  (SG0875) is gradually established on moving from  $\sigma_b$  at 200 to 400 °C (Figure 8(b)) to  $\sigma_t$  from 400 to 800 °C (Figure 8(a)). For series one this peak takes over from the trend of increasing conductivity as Sm content increases that is seen at the lower temperatures. SG0875 has equal highest total conductivity with SG050 at 500 °C but surpasses it at 600 °C and above. There is a decrease in  $\sigma_t$  as dopant concentration increases after the peak for SG0875 and this becomes less marked as temperature increases from 400 to 800 °C. This can be explained by the increased dissociation of defect complexes as temperature increases. Samples with a higher dopant concentration and hence a greater oxygen vacancy concentration will form more defect complexes which hinder oxygen ion mobility and reduce conductivity.<sup>30</sup> As temperature increases, these defect complexes dissociate and release these vacancies, which can then contribute to oxygen ion conductivity. This is the reason that the difference between the  $\sigma_t$  values for SG100 and SG125 decreased as temperature increased from 400 to 800 °C. For series two, the constant oxygen vacancy concentration meant that the overall variation in conductivity was smaller than for series one. Nevertheless, there is a notable (particularly at 800 °C) increase in  $\sigma_t$  from G175 to G140 corresponding to the onset of Sm-Gd co-doping. In Figure

8(c), the variations in  $\sigma_{gb}$  with Sm content did not match those of  $\sigma_b$ . The  $\sigma_{gb}$  showed a minimum at SG0875 for series two at all temperatures, rather than a maximum, as was the case for  $\sigma_b$ . Since  $\sigma_{gb}$  was generally much greater than  $\sigma_b$ , however, this had little effect on  $\sigma_t$ .

Dikmen and co-workers have also reported on Sm-Gd co-doping in  $Ce_{0.8}Gd_{0.2-x}Sm_xO_{2.6}$  ( $x = 0-0.1$ ) and have demonstrated that it can improve the electrical performance of ceria-based electrolytes.<sup>19,32</sup> The ionic conductivity reported for  $Ce_{0.8}Sm_{0.18}Gd_{0.02}O_{1.9}$  at 700 °C ( $2.88 \text{ S m}^{-1}$ ) was 40 % lower than that of the most similar sample,  $Ce_{0.825}Sm_{0.14}Gd_{0.035}O_{1.9125}$  ( $4.77 \text{ S m}^{-1}$ ), synthesised in the present study.<sup>32</sup> This is likely to be related to the different total dopant concentrations, 20 vs. 17.5 mol %, and the different relative concentrations of individual dopants, 10 vs. 20 % Gd. The higher values of the present study may also be attributed in part to the different synthesis methods (citrate complexation rather than hydrothermal) which is known to give high purity materials and therefore high  $\sigma_{gb}$ . A further study by Dikmen looked in greater detail at varying Sm:Gd ratios, from 0:100 to 50:50.<sup>19</sup> The authors found that total conductivity increased as the relative Sm concentration increased, with a decreasing rate of change as the composition approached 50:50. Although the actual compositions are different in this and the present study, both studies indicate that Sm:Gd = 50:50 gives the greatest conductivity enhancement. The most directly comparable sample is for 20 % Sm:  $Ce_{0.8}Sm_{0.04}Gd_{0.16}O_{1.9}$  gave a total conductivity of  $3.77 \text{ S m}^{-1}$  at 700 °C whereas, in the present study,  $Ce_{0.8125}Sm_{0.035}Gd_{0.14}O_{1.9125}$  (G140) gave a 27 % higher value of  $4.78 \text{ S m}^{-1}$  at the same temperature.<sup>19</sup> This demonstrates the benefits of using a total concentration of 17.5 rather than 20 mol % for Sm-Gd co-doped ceria electrolytes.

Winck and co-workers also investigated the Sm-Gd co-doped ceria system in  $Ce_{0.8}Sm_{0.2-x}Gd_xO_{1.9}$  ( $x = 0, 0.05, 0.1$ ) made using the Pechini method.<sup>33</sup> They found an increase in  $\sigma_b$  on addition of Gd and they rationalised this in terms of the decrease in deformation of the crystal lattice with increased amounts of the smaller dopant cation ( $Gd^{3+}$ ) leading to a consequent decrease in the height of the barrier to oxygen ion migration.<sup>33</sup> This, they claimed, was because less lattice expansion would result in shorter ion jump distances. However, these authors did not investigate compositions with Sm:Gd ratios lower than 50:50 and, furthermore, the behaviour was not monotonic since they observed a maximum in  $\sigma_b$  for the intermediate composition, with  $x = 0.05$ . Their sample,  $Ce_{0.8}Sm_{0.1}Gd_{0.1}O_{1.9}$ , gave a  $\sigma_t$  value at 600 °C of  $0.797 \text{ S m}^{-1}$ , which is 56 % lower than the value for the sample of the same composition in this work,  $1.80 \text{ S m}^{-1}$ . The difference can be attributed to the different synthesis methods used. Using the Pechini method, Winck and co-workers found that  $\sigma_{gb}$  was significantly lower than  $\sigma_b$  such that  $\sigma_{gb}$  (determined by microstructural characteristics) dominated  $\sigma_t$ , which was not the case for the citrate complexation method used in this work.

Arabaci looked at the Sm-Gd co-doped system and found that the composition  $Ce_{0.8}Sm_{0.12}Gd_{0.08}O_{1.9}$  had a  $\sigma_t$  of  $5.28 \text{ S m}^{-1}$  at 750 °C.<sup>34</sup> Separate  $\sigma_{gb}$  values were not reported but, as in the present work, a citrate-nitrate complexation process was used so the grain boundary resistances are likely to be lower than in other studies. The most directly comparable sample in the present work is G070 which also had a Sm:Gd ratio of 60:40. G070 had a  $\sigma_t$  of  $6.47 \text{ S m}^{-1}$  at 750 °C which is 23 % higher than the value Arabaci

obtained for  $\text{Ce}_{0.8}\text{Sm}_{0.12}\text{Gd}_{0.08}\text{O}_{1.9}$ . This again demonstrates the benefits of using a total concentration of 17.5 rather than 20 mol % for Sm-Gd co-doped ceria electrolytes.

### 3.3.3. Activation Energies and Pre-Exponential Factors

In Figure S2, the plots of total conductivity contain a change in gradient at around 500 °C. This is a general and well-known effect for ionically-conducting aliovalently-doped ceramics.<sup>35</sup> At low temperatures, below the inflection, defects are associated to form defect clusters. At high temperatures, above the inflection point, these dissociate and the defect cluster concentration is assumed to be negligible. Therefore, the gradient above the inflection was used to calculate the migration enthalpy of the oxygen vacancies,  $\Delta H_m$ , whilst the gradient below the inflection point gave the sum of the migration enthalpy and the defect association enthalpy,  $\Delta H_m + \Delta H_a$ . Values for the pre-exponential constant,  $\sigma_0$ , were obtained by extrapolating the low temperature branch of the Arrhenius plots to the y-axis and these are presented in Figure 9(a) and (b). Values of  $\Delta H_m$ ,  $\Delta H_a$ ,  $E_t$  ( $= \Delta H_m + \Delta H_a$ ), obtained from data below 500 °C) as well as activation energies for bulk and grain boundary conductivity-  $E_b$  and  $E_{gb}$ - were obtained and are plotted as a function of mole fraction of Sm in Figure 9(c) and (d).

The plot of  $\sigma_0$  for series one shows a sharp increase with increase in overall dopant concentration (Gd and Sm increase in parallel) and hence, with increase in oxygen vacancy (charge carrier) concentration. This can be understood in terms of the relationship between  $\sigma_0$  and oxygen vacancy concentration. In series two, the correlation of  $\sigma_0$  with increasing Sm content is negative and approximately linear. This trend is subtler than for series one, since the total dopant concentration is kept constant in series two. As well as the number of oxygen vacancies, enhanced configuration entropy - which is reported to arise from an increase in the number of equal-energy sites lowering activation energy and facilitating oxide ion diffusion - is said to increase  $\sigma_0$ .<sup>30</sup> According to this approach, there should be an increase in  $\sigma_0$  as the Sm:Gd ratio increases in series two. However, in reality a decrease was seen which may be directly or indirectly linked to the increase in average ionic radius as was discussed in recent work by the present authors.<sup>4</sup>

The pre-exponential factors of ceria electrolytes have not been widely studied but those calculated for the compositions presented here are approximately two orders of magnitude higher than those reported by Kasse and co-workers for  $\text{Ce}_{0.9}\text{Sm}_x\text{Nd}_y\text{O}_{2.5}$  ( $x + y = 0.1$ ,  $x = 0 - 0.1$ ).<sup>36</sup> These authors gave log(pre-exponential) values of between 6.73 and 7.00 for their sample series compared to the values of 8.25 – 9.24 presented here.<sup>36</sup> The differences are likely to be due to the different dopants used. The comparable bulk conductivities they reported therefore must arise from their lower activation energy (particularly association enthalpy) values.<sup>36</sup> This emphasises the importance of both increasing  $\sigma_0$  and decreasing activation energy to maximise conductivity. Tuller and Nowick reported a  $\sigma_0$  for  $\text{Ce}_{0.95}\text{Y}_{0.05}\text{O}_{1.975}$  ( $1.9 \times 10^7$ ) which is at least one order of magnitude smaller than those presented here.<sup>37</sup> This can be partly attributed to the low dopant concentration used because of the positive relationship between  $\sigma_0$  and the number of oxygen vacancies, as seen for series one. However, even if Figure 9(a) is extrapolated down to a total dopant concentration of

Formatted: Highlight

Formatted: Highlight

Formatted: Highlight

5 mol % (*i.e.*: a Sm mole fraction of 0.025), the estimated  $\sigma_0$  is still higher than that reported for  $\text{Ce}_{0.95}\text{Y}_{0.05}\text{O}_{1.975}$ , indicating that dopant identity is also important in determining the value of  $\sigma_0$ .

The general trend in the activation energies,  $E_b$ ,  $E_{gb}$  and  $E_t$ , for series one is apparent in Figure 9(c) and is a close-to-linear increase with increasing total dopant concentration. Values of  $E_b$  and  $E_t$  are very similar, except for a deviation in  $E_b$  at dilute dopant concentrations, where the contribution of  $\sigma_{gb}$  becomes non-negligible because of the unusually high  $\sigma_b$  at low temperatures. The values of  $E_{gb}$  were generally higher than  $E_b$  and  $E_t$  but all three converged as dopant concentration increased. For series two (Figure 9(b)), there is a close-to-linear decrease with increasing Sm:Gd ratio for  $E_b$  and  $E_t$  but  $E_{gb}$  remains higher and almost constant across the range of Sm:Gd ratio.  $E_b$  and  $E_t$  are more closely matched than for series one since here  $\sigma_{gb}$  is always much greater than  $\sigma_b$  and so has negligible effect on  $\sigma_t$ . The differences in trends between the two series is understandable since series one involves an increase in dopant and oxygen vacancy concentration whilst, in series two, an increase in Sm:Gd ratio takes place but with total dopant and oxygen vacancy concentrations held constant.

Cioateră *et al* reported  $E_b$  and  $E_{gb}$  values for  $\text{Ce}_{0.85}\text{Gd}_{0.05}\text{Sm}_{0.1}\text{O}_{2.6}$  at temperatures below 450 °C of 0.86/0.89 eV and 1.48/1.36 eV, respectively (two values were reported because two synthesis methods were used).<sup>38</sup> This composition contained 33 % Gd as dopant which is closest to G070 (40 % Gd) in the present study. G070 gave  $E_b$  and  $E_{gb}$  values of 0.82 and 0.93 eV respectively. Whilst the  $E_b$  values are similar,  $E_{gb}$  is significantly lower for G070. This is likely to be because the citrate-nitrate synthesis method employed here gives high purity materials with low grain boundary resistances whereas the impedance spectra of Cioateră *et al* showed large grain boundary arcs.<sup>38</sup>

Winck and co-workers reported  $E_b$  and  $E_{gb}$  values for  $\text{Ce}_{0.8}\text{Sm}_{0.1}\text{Gd}_{0.1}\text{O}_{1.9}$  of 1.072 and 1.229 eV respectively, slightly **higher** than the corresponding values of 0.93 and 1.00 eV for the sample of the same composition in this work.<sup>33</sup> These authors also reported a total activation enthalpy of 1.143 eV for  $\text{Ce}_{0.8}\text{Sm}_{0.1}\text{Gd}_{0.1}\text{O}_{1.9}$  **but separate total activation energies at high and low temperatures were not resolved.** **It is therefore assumed** that this value corresponds to the activation energy at low temperature ( $\Delta H_a + \Delta H_m$ ) as it is roughly comparable to the 0.93 eV obtained for the sample of the same composition here. The differences are likely to result from the different synthesis methods used. The Pechini method used by Winck and co-workers resulted in a total activation energy more influenced by grain boundaries than is the case for the high purity products resulting from the citrate complexation method used here.<sup>33</sup> This is exemplified by the low temperature activation energy for SG100 being the same as  $E_b$  (to two significant figures) whereas the total activation energy reported by Winck and co-workers for  $\text{Ce}_{0.8}\text{Sm}_{0.1}\text{Gd}_{0.1}\text{O}_{1.9}$  is 0.071 eV higher than their  $E_b$  value.<sup>33</sup>

Spiridigliozzi and co-workers investigated various compositions of Gd-doped ceria (5 – 20 mol %) using flash sintering at 700 °C and noted a minimum total activation energy at 10 mol % Gd.<sup>39</sup> Although the composition equivalent to G175 was not investigated, two samples after the minimum at 10 mol % Gd ( $\text{Ce}_{0.85}\text{Gd}_{0.15}\text{O}_{1.925}$  and  $\text{Ce}_{0.8}\text{Gd}_{0.2}\text{O}_{1.9}$ ), which have dopant concentrations either side of 17.5 mol % were. These gave total activation energy ( $\Delta H_a + \Delta H_m$ ) values of 1.04 and 1.10 eV, respectively. These values are

Formatted: Highlight

Formatted: Highlight

Formatted: Highlight

Formatted: Highlight

slightly higher than the values of 0.90, 0.85 and 0.93 eV obtained here for G175, SG075 and SG100 (the latter two samples having

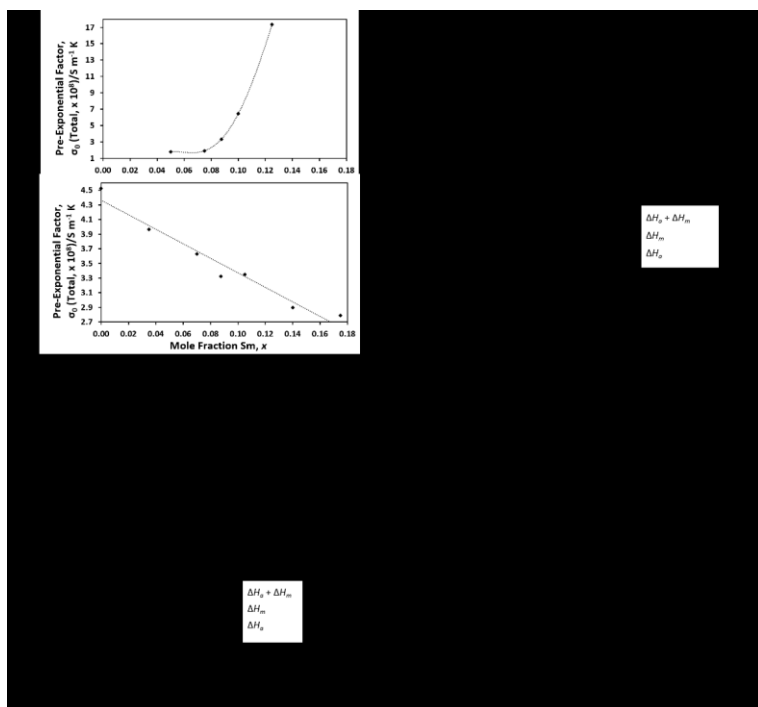


Figure 9. Pre-exponential factor as a function of mole fraction of Sm,  $x$ , for a) series one,  $\text{Ce}_{1-x}\text{Sm}_x\text{Gd}_x\text{O}_{2-x}$  and b) series two,  $\text{Ce}_{0.825}\text{Sm}_x\text{Gd}_{0.175}\text{O}_{1.9125}$ . Activation energies for bulk and grain boundary processes and total conductivity below ( $\Delta H_b + \Delta H_m$ ) and above ( $\Delta H_m$ ) 500 °C and  $\Delta H_b$  for c) series one and d) series two samples. See text for details. Meyer-Neldel plots for the bulk material of e) series one and f) series two.

the same total dopant concentrations as  $\text{Ce}_{0.85}\text{Gd}_{0.15}\text{O}_{1.925}$  and  $\text{Ce}_{0.8}\text{Gd}_{0.2}\text{O}_{1.9}$ , respectively. As well as these materials being only singly-doped, the activation energies are likely to be influenced to some extent by the different synthesis and sintering methods used: co-precipitation and flash sintering compared to citrate complexation and conventional sintering.

The increasing trend in  $\Delta H_b$  with increasing total dopant concentration in series one can be explained as the corresponding increase in the number of defect clusters incorporating greater numbers of dopant ions and oxygen vacancies. The decreasing trend in  $\Delta H_b$  in series two can be attributed to the increasing Sm:Gd ratio where the larger  $\text{Sm}^{3+}$  ion may give rise to more weakly bound defect complexes. The trends in  $\Delta H_m$  indicate that oxygen ion mobility is disfavoured as total dopant concentration increases for series one, and is also mildly disfavoured as Sm:Gd ratio increases in series two. In series one, values for  $\Delta H_m$  for the two lowest dopant concentrations are higher than expected because of the deviations in  $E_b$  for these compositions, as discussed above. The differences in the trends in  $\Delta H_b$  for the two series result in  $E_b$  increasing in series one and decreasing in series two, as Sm content increased. It is interesting that the trends in  $\Delta H_b$  shown in Figure 9(c) and (d) are reflected in the corresponding trends in strength

of coupling parameter for series one and two discussed below in connection with the Meyer-Neldel plots of Figure 9(e) and (f). These two phenomena are expected to be closely related.

In computational work, Andersson *et al* proposed that the ideal dopant for ceria electrolytes should have an effective atomic number between 61 (Pm) and 62 (Sm).<sup>15</sup> This is because this atomic number gave the lowest sum of  $\Delta H_m$  and  $\Delta H_o$  for a dopant concentration of 4.2 %. This effective atomic number is equivalent to an average dopant ionic radius of 1.086 Å.<sup>12</sup> In the present experimental study, G000 had the closest effective atomic number and average dopant ionic radius **to this ideal as determined by Andersson *et al*'s value and** did show the lowest total activation energy (the sum of  $\Delta H_m$  and  $\Delta H_o$ ) of series two (0.87 eV).<sup>15</sup> However, SG050 (1.066 Å) had the lowest total activation energy of both series one and two (0.83 eV). This is likely to be because SG050 had the lowest dopant and oxygen vacancy concentrations and hence the lowest defect cluster concentration. This is despite SG050 having an average dopant ionic radius further from *the Andersson *et al*'s ideal* than G000. Therefore, it is important to consider both average dopant ionic radius and total dopant concentration when designing ceria electrolytes for IT-SOFCs.

Formatted: Highlight

Formatted: Font: Italic

Kilner gave experimental (0.17 eV) and calculated (0.13 eV) values of  $\Delta H_o$  of GDC (with 10-15 mole% Gd).<sup>8</sup> The latter agrees with that for GDC given by Steele.<sup>35</sup> Here, G175 is the sample with the closest composition, but has a higher  $\Delta H_o$ , of 0.34 eV. Even the lowest  $\Delta H_o$  value of the present study, 0.23 eV for SG050, is higher than the above literature values. The computational calculations of Minervini and co-workers gave  $\Delta H_o$  for GDC of 0.38 eV (close to the 0.34 eV obtained here for G175).<sup>11</sup> Faber and co-workers obtained  $\Delta H_o$  values by extrapolating their data to infinite dopant dilution, with the assumption that  $\Delta H_m$  was 0.5 eV (the average obtained in the present work was 0.61 eV).<sup>40</sup> For Gd as a dopant, this gave a  $\Delta H_o$  value of 0.32 eV which is also close to the 0.34 eV acquired here for G175.

The  $\Delta H_m$  values in this study are similar to the values at the lower end of the range (approximately 0.64 eV to 0.86 eV) found by Omar *et al* for different singly doped ceria systems.<sup>16</sup> The computational work by Andersson *et al* mentioned above reported  $\Delta H_m$  values **of about 0.38**, 0.40, 0.39, 0.33 eV for doping with Nd, Pm, Sm and Gd, respectively.<sup>15</sup> These values were calculated for the dopant ions NN to each other, so this may account for these computational  $\Delta H_m$  values being lower than those in the present study. The  $\Delta H_m$  values calculated by Andersson *et al* did not include other vacancy migration pathways of higher energy (*i.e.*: for dopants ions further apart, in any other configuration than NN) which are likely also to make some contribution. Arabaci reported a  $\Delta H_m$  value of 0.60 eV for  $\text{Ce}_{0.8}\text{Sm}_{0.12}\text{Gd}_{0.08}\text{O}_{1.9}$  which is only slightly higher than the 0.55 eV obtained here for the equivalent sample, G105, where Gd is also 40 % of the dopant content, with the difference likely due to the different overall dopant concentrations.<sup>34</sup>

Formatted: Highlight

Poorly conducting grain boundaries would strongly affect total conductivity values, causing inaccuracies in the  $\Delta H_m$  and  $\Delta H_o$  values acquired from them. However, this is not expected to be the case in this work since  $\sigma_{gb}$  is generally much higher than  $\sigma_b$ . This is the result of using the solution-based citrate-nitrate synthesis method, which allows the preparation of materials with low impurity levels. This method is also expected to promote atomic mixing of the host (Ce) and dopant (Sm and Gd) cations whereas the

conventional ceramic 'shake-and-bake' method may lead to the production of nanodomains with different dopant concentrations due to its reliance on inter-diffusion of the cations of the starting oxides. This absence of nanodomains is supported by the absence of additional spots in the diffraction pattern presented in Figure 2(e).

If a system obeys the Meyer-Neldel rule, a linear relationship exists between the log of the pre-exponential factor and  $E_a$  (Equation 3).<sup>41</sup> It is interesting that both series one and two closely exhibit this relationship for the bulk material, having  $\alpha$  and  $\beta$  values of 5.40 and 3.77, respectively, for series one and 6.63 and 2.75, respectively, for series two (see Figure 9(e) and (f)). The Meyer-Neldel rule states that there is a temperature, often around 475 °C, at which conductivity converges and becomes independent of dopant concentration.<sup>42</sup> Total dopant concentration is constant for series two, but a convergence in conductivity is observed for bulk and total conductivities for series one (where total dopant concentration varies) as temperature increases, particularly at around 500 °C and above. This implies less of a dependence, if not complete independence, on dopant concentration.

$$\log \sigma_0 = \alpha \Delta H + \beta \quad (3)$$

The physical meaning of the Meyer-Neldel rule has been discussed by Ngai using the coupling model.<sup>43</sup> The key part of this model is the existence of a microscopic time which is independent of temperature. Before this time, the interactions between ions have no effect on the dynamics of the ions and the attempt frequency for ion hopping is equal to the vibrational frequency of the ion. After this time, anharmonic interactions slow down the relaxation of the ions. The rate of this slowing down is quantified by a coupling parameter. The crossover time of the transition between these two regimes, which can be gradual, has been reported to be consistent with high frequency AC conductivity measurements of ionic conductors.<sup>44</sup> Since the coupling factor influences the relaxation time of the ions it also influences the ionic conductivity and the associated activation energy. By comparing these two relationships, it is possible to arrive at the expression in Equation 3. The coupling factor depends on the concentration of the conducting ion, the dielectric constant and the structure of the material since these factors influence the effective Coulombic interactions between the diffusing ions. According to the rule, as the coupling factor increases, both the activation energy and the pre-exponential factor for conduction increase. Considering Figure 9(e) and (f), inter-ionic coupling would therefore be expected to increase as total dopant concentration increased in series one and as Sm/Gd ratio decreased in series two. The former makes sense since increased dopant concentration would lead to increased charge carrier concentration and, therefore, to stronger overall interactions between them. The latter observation supports the idea that the presence of Sm promotes less inter-ion coupling. In this model, the temperature at which conductivity becomes independent of dopant concentration is also the transition point (change in gradient) in the Arrhenius plots in Figure S2. This temperature corresponds to an order-disorder or associated-disassociated transition in the oxygen ion sublattice where above this temperature, the oxygen ions are no longer trapped by cation defects on specific lattice sites but become mobile.<sup>45,42</sup> Few other ionic conductors have been studied using the Meyer-Neldel rule.<sup>46</sup>

Conductivity is not only dependent on activation energies, but also on the pre-exponential factor. This means that maximum conductivity may not correspond to a minimum in activation energy. This is seen here for SG0875 which had the highest conductivity at intermediate temperatures, despite it not having the lowest corresponding activation energies or migration or association enthalpies or the highest pre-exponential factor. For series one there is an increase in both bulk activation energy and pre-exponential factor as dopant ([Sm] + [Gd]) content increases. The increase in bulk activation energy can be attributed to the increasing degree of defect association as dopant and oxygen vacancy concentrations increase (reflected in an increase in (apparent) association enthalpy) and to the accompanying increase in migration enthalpy. The increase in the pre-exponential factor is simply related to the large increase in the concentration of oxygen vacancy charge carriers with increasing dopant concentration. For series two there is a decrease in both bulk activation energy and in pre-exponential factor as the Sm/Gd ratio increases. This decrease in bulk activation energy is the result of the modest increase in migration enthalpy,  $\Delta H_m$ , and a decrease in association enthalpy,  $\Delta H_a$ . The latter is attributed to the weakening of the interaction between the trivalent dopant ions and oxygen vacancies as the proportion of the larger  $\text{Sm}^{3+}$  ion increases. The trend in pre-exponential constant for series two is subtle, since overall dopant concentration is kept constant, but shows a roughly linear decrease as Sm content increases. This may be a consequence of increasing average ionic radius (or lattice constant) which also determined the trend in pre-exponential factor for the samples studied in previous work.<sup>4</sup> In both series, the interplay between activation energy and pre-exponential factor resulted in the intermediate composition, SG0875, having the highest conductivity over the temperature range of interest for SOFCs. Other reports have also shown that co-doped ceria electrolytes can have higher conductivities despite also having higher activation energies.<sup>47</sup>

### Conclusions

A citrate complexation process was used to prepare successfully two series of high purity electrolyte nanopowders:  $\text{Ce}_{1-x}\text{Sm}_x\text{Gd}_x\text{O}_{2-x}$  where  $x = 0.125, 0.1, 0.0875, 0.075$  or  $0.05$  (series one) and  $\text{Ce}_{0.825}\text{Sm}_x\text{Gd}_{0.175-x}\text{O}_{1.9125}$  where  $x = 0.175, 0.14, 0.105, 0.0875, 0.07, 0.035$  or  $0$  (series two). These nanopowders - and dense sintered pellets made from them - were used to study the effect of total dopant concentration and Sm:Gd ratio on microstructure and ionic conductivity in ceria co-doped with Sm and Gd. This is the first time such an extensive study of the Sm-Gd co-dopant system has been reported.

The nanopowders had crystallite sizes between 46 and 101 Å and were high-purity, single-phase cubic fluorite materials which adhered to Vegard's Law. In the dense pellets, no simple trend in relative density with dopant content was observed in either series. This was also the case for average grain diameter for series one. However, for series two, grain diameter decreased on the first addition of Sm, and then increased monotonically with Sm content.

Impedance spectroscopy was carried out on the dense pellets. Grain boundary conductivity was much higher than bulk conductivity in general. This was linked to the high sample purity achievable using the citrate-nitrate preparation method. Total conductivities of the samples compared favourably with literature values.

A total dopant concentration of 17.5 mol % and a Sm:Gd ratio of 50:50 gave the highest total conductivity at temperatures of 550 °C and above. Multiple doping with Sm and Gd was found to be beneficial compared to the singly-doped parent materials for three of the  $\text{Ce}_{0.825}\text{Sm}_x\text{Gd}_{0.175-x}\text{O}_{1.9125}$  compositions ( $x = 0.0875$ ,  $x = 0.07$  and  $x = 0.035$ ) but averaging for two ( $x = 0.14$  and  $x = 0.105$ ) at IT-SOFC working temperatures. There were variations in these trends with temperature. These variations are attributed to the interplay between the activation energies of defect cluster association ( $\Delta H_a$ ) and oxygen ion migration ( $\Delta H_m$ ), and the pre-exponential factor. In order to maximise conductivity in cerias with Sm and Gd co-doping, Sm:Gd ratios of 50:50 should be used. SG0875 had significantly higher  $\sigma_t$  than samples with different total dopant concentrations (series one) between 550 and 900 °C and higher  $\sigma_t$  than samples with different Sm:Gd ratios (series two) between 450 and 900 °C. It had a  $\sigma_t$  value of  $2.23 \text{ S m}^{-1}$  at 600 °C which is 24 % higher than the  $1.80 \text{ S m}^{-1}$  for SG100 at the same temperature. This high conductivity was also stable in extended tests. This composition is therefore of considerable interest for application in IT-SOFCs.

In series one at low temperatures, total conductivity clearly increased as dopant content decreased. This was interpreted as being caused by the decreased trapping of oxygen ion vacancies- making them unavailable for conduction- at dilute dopant concentrations. The conductivity trends for series two were highly temperature-dependent but less easily interpreted due to the constant dopant concentration and variation of Sm:Gd ratio only. Nevertheless, there was a general trend of increasing conductivity with increasing Sm content at low temperatures which may be linked to  $\text{Sm}^{3+}$  having no NN/NNN vacancy position preference.<sup>15</sup>

The pre-exponential constant for series one showed an exponential increase with increase in overall dopant concentration due to the relationship between pre-exponential constant and charge carrier concentration. In series two, the subtler change in pre-exponential constant (due to the constant total dopant concentration) showed a negative, approximately linear correlation with increasing Sm content.

Association and migration enthalpies had respective values of between 0.23 (SG050) and 0.34 eV (SG100) and between 0.55 (G105) and 0.72 eV (SG125). The trends in these enthalpies were discussed with reference to current models of doped cerias. This demonstrated the importance of considering both dopant ratios and the corresponding average dopant ionic radius as well as total dopant concentration, and hence defect associate concentration, when optimising ceria electrolytes for IT-SOFCs. In series one both bulk activation energy and pre-exponential constant increased with increasing dopant concentration, while in series two, both decreased.

A clear maximum in bulk capacitance was seen for SG0875, the most conducting sample at high temperatures. A model is proposed to link these two findings.

Both series showed close agreement with the Meyer-Neldel rule and this was discussed in terms of the changing strength of coupling between ionic charge carriers in these materials. According to this model, coupling strength increased as total dopant concentration increased in series one and decreased as Sm/Gd ratio increased in series two.

It is hoped that the detailed results and interpretation presented here will contribute to both the design and computational modelling of doped ceria ionic conductors.

### Conflicts of interest

There are no conflicts to declare.

### Acknowledgements

The authors thank the University of St Andrews and the UK Engineering and Physical Sciences Research Council for the PhD studentship for AVC-A (grant code: EP/M506631/1). Electron microscopy was performed at the Electron Microscope Facility, University of St Andrews.

### Notes and references

- 1 Y. Guo, M. Bessaa, S. Aguado, M. C. Steil, D. Rembelski, M. Rieu, J.-P. Viricelle, N. Benameur, C. Guizard, C. Tardivat, P. Vernoux and D. Farrusseng, *Energy Environ. Sci.*, 2013, **6**, 2119–2123.
- 2 E. D. Wachsman, C. A. Marlowe and K. T. Lee, *Energy Environ. Sci.*, 2012, **5**, 5498–5509.
- 3 H. Qin, Z. Zhu, Q. Liu, Y. Jing, R. Raza, S. Imran, M. Singh, G. Abbas and B. Zhu, *Energy Environ. Sci.*, 2011, **4**, 1273–1276.
- 4 J. C. Ruiz-Morales, D. Marrero-López, M. Gálvez-Sánchez, J. Canales-Vázquez, C. Savaniu and S. N. Savvin, *Energy Environ. Sci.*, 2010, **3**, 1670–1681.
- 5 A. B. Stambouli and E. Traversa, *Renew. Sustain. Energy Rev.*, 2002, **6**, 433–455.
- 6 T. Ishii and Y. Tajima, *J. Electrochem. Soc.*, 1994, **141**, 3450–3453.
- 7 Y. Mishima, H. Mitsuyasu, M. Ohtaki and K. Eguchi, *J. Electrochem. Soc.*, 1998, **145**, 1004–1007.
- 8 J. Kilner, *Solid State Ionics*, 2000, **129**, 13–23.
- 9 J. B. Goodenough, *Annu. Rev. Mater. Res.*, 2003, **33**, 91.
- 10 H. Inaba and H. Tagawa, *Solid State Ionics*, 1996, **83**, 1–16.
- 11 L. Minervini, M. O. Zacate and R. W. Grimes, *Solid State Ionics*, 1999, **116**, 339–349.
- 12 R. Shannon, *Acta Crystallogr. Sect. A*, 1976, **32**, 751–767.
- 13 M. Mogensen, D. Lybye, N. Bonanos, P. V. Hendriksen and F. W. Poulsen, *Solid State Ionics*, 2004, **174**, 279–286.
- 14 S. Omar, E. D. Wachsman, J. C. Nino, *Solid State Ionics*, 2006, **177**, 3199–3203.
- 15 D. A. Andersson, S. I. Simak, N. V. Skorodumova, I. A. Abrikosov and B. Johansson, *Proc. Natl. Acad. Sci. U. S. A.*, 2006, **103**, 3518–3521.
- 16 S. Omar, E. D. Wachsman, J. L. Jones and J. C. Nino, *J. Am. Ceram. Soc.*, 2009, **92**, 2674–2681.
- 17 M. Burbano, S. Nadin, D. Marrocchelli, M. Salanne and G. W. Watson, *Phys. Chem. Chem. Phys.*, 2014, **16**, 8320–8331.
- 18 F.-Y. Wang, B.-Z. Wan and S. Cheng, *J. Solid State Electrochem.*, 2004, **9**, 168–173.
- 19 S. Dikmen, *J. Alloys Compd.*, 2010, **491**, 106–112.
- 20 W. Zajac and J. Molenda, *Solid State Ionics*, 2008, **179**, 154–158.
- 21 R. O. Fuentes and R. T. Baker, *J. Power Sources*, 2009, **186**, 268–277.
- 22 A. R. Denton and N. W. Ashcroft, *Phys. Rev. A*, 1991, **43**, 3161–3164.

- 23 H. Klug and L. Alexander, *X-Ray Diffraction Procedures for Polycrystalline and Amorphous Materials*, John Wiley, New York, 1974.
- 24 M. R. Kosinski and R. T. Baker, *J. Power Sources*, 2011, **196**, 2498–2512.
- 25 A. V. Coles-Aldridge and R. T. Baker, *Solid State Ionics*, 2018, **316**, 9–19.
- 26 Z. Tianshu, P. Hing, H. Huang and J. Kilner, *Solid State Ionics*, 2002, **148**, 567.
- 27 Y. Liu, B. Li, X. Wei and W. Pan, *J. Am. Ceram. Soc.*, 2008, **91**, 3926–3930.
- 28 M. R. Kosinski, University of St Andrews, 2011.
- 29 T. Sherwood, University of St Andrews, 2016.
- 30 S. Omar, E. Wachsman and J. Nino, *Solid State Ionics*, 2008, **178**, 1890–1897.
- 31 K. Venkataramana, C. Madhuri, Y. Suresh Reddy, G. Bhikshamaiah and C. Vishnuvardhan Reddy, *J. Alloys Compd.*, 2017, **719**, 97–107.
- 32 S. Dikmen, H. Aslanbay, E. Dikmen and O. Şahin, *J. Power Sources*, 2010, **195**, 2488–2495.
- 33 L. B. Winck, J. L. de Almeida Ferreira, J. M. G. Martinez, J. A. Araujo, A. C. M. Rodrigues and C. R. M. da Silva, *Ceram. Int.*, 2017, **43**, 16408–16415.
- 34 A. Arabaci, *Metall. Mater. Trans. A Phys. Metall. Mater. Sci.*, 2017, **48**, 2282–2288.
- 35 B. C. H. Steele, *Solid State Ionics*, 2000, **129**, 95–110.
- 36 R. M. Kasse and J. C. Nino, *J. Alloys Compd.*, 2013, **575**, 399–402.
- 37 H. L. Tuller and A. S. Nowick, *J. Electrochem. Soc.*, 1975, **122**, 255–259.
- 38 N. Cioatera, V. Părvulescu, A. Rolle and R. N. Vannier, *Ceram. Int.*, 2012, **38**, 5461–5468.
- 39 L. Spiridigliozzi, M. Biesuz, G. Dell'Agli, E. Di Bartolomeo, F. Zurlo and V. M. Sglavo, *J. Mater. Sci.*, 2017, **52**, 7479–7488.
- 40 J. Faber, C. Geoffroy, A. Roux, A. Sylvestre and P. Abelard, *Appl. Phys. A*, 1989, **49**, 225–232.
- 41 I. Stephens and J. Kilner, *Solid State Ionics*, 2006, **177**, 669–676.
- 42 A. S. Nowick, W. K. Lee and H. Jain, *Solid State Ionics*, 1988, **28**, 89.
- 43 K. Ngai, *Solid State Ionics*, 1998, **105**, 231–235.
- 44 K. Ngai, *Solid State Ionics*, 1998, **105**, 225–230.
- 45 D. P. Almond and A. R. West, *Solid State Ionics*, 1987, **23**, 27.
- 46 L. Aneflous, J. A. Musso, S. Villain, J. R. Gavarri and H. Benyaich, *J. Solid State Chem.*, 2004, **177**, 856–865.
- 47 X. Sha, Z. Lü, X. Huang, J. Miao, Z. Ding, X. Xin and W. Su, *J. Alloys Compd.*, 2007, **428**, 59–64.